RESEARCH ARTICLE
SPACE PHYSICS: MAGNETOSPHERIC PHYSICS

Earth and Planetary Physics
8: 47–58, 2024
doi: 10.26464/epp2023053

Global hybrid simulations of soft X-ray emissions in the Earth's magnetosheath

Jin Guo[1,2], TianRan Sun[4*], San Lu[1,2,3*], QuanMing Lu[1,2,3], Yu Lin[5], XueYi Wang[5], Chi Wang[4], RongSheng Wang[1,2,3], and Kai Huang[1,2,3]

[1]School of Earth and Space Sciences, University of Science and Technology of China, Hefei 230026, China;

[2]CAS Center for Excellence in Comparative Planetology/CAS Key Lab of Geospace Environment, University of Science and Technology of China, Hefei 230026, China;

[3]Collaborative Innovation Center of Astronautical Science and Technology, Harbin 150001, China;

[4]National Space Science Center, Chinese Academy of Sciences, Beijing 100190, China;

[5]Physics Department, Auburn University, Auburn, AL, USA

Key Points:

- 3-D global hybrid-PIC simulation is applied to estimate the soft X-ray imaging of Earth's magnetopause under different solar wind conditions.
- Plasma waves and local structures in the magnetosheath lead to large amplitude fluctuations of X-ray emissivity.
- The influence of magnetosheath fluctuations on identifying magnetopause boundary in the X-ray image is limited under different solar wind conditions and viewing geometries.

Citation: Guo, J., Sun, T. R., Lu, S., Lu, Q. M., Lin, Y., Wang, X. Y., Wang, C., Wang, R. S., and Huang, K. (2024). Global hybrid simulations of soft X-ray emissions in the Earth's magnetosheath. *Earth Planet. Phys.*, *8*(1), 47–58. http://doi.org/10.26464/epp2023053

Abstract: Earth's magnetopause is a thin boundary separating the shocked solar wind plasma from the magnetospheric plasmas, and it is also the boundary of the solar wind energy transport to the magnetosphere. Soft X-ray imaging allows investigation of the large-scale magnetopause by providing a two-dimensional (2-D) global view from a satellite. By performing 3-D global hybrid-particle-in-cell (hybrid-PIC) simulations, we obtain soft X-ray images of Earth's magnetopause under different solar wind conditions, such as different plasma densities and directions of the southward interplanetary magnetic field. In all cases, magnetic reconnection occurs at low latitude magnetopause. The soft X-ray images observed by a hypothetical satellite are shown, with all of the following identified: the boundary of the magnetopause, the cusps, and the magnetosheath. Local X-ray emissivity in the magnetosheath is characterized by large amplitude fluctuations (up to 160%); however, the maximum line-of-sight-integrated X-ray intensity matches the tangent directions of the magnetopause well, indicating that these fluctuations have limited impact on identifying the magnetopause boundary in the X-ray images. Moreover, the magnetopause boundary can be identified using multiple viewing geometries. We also find that solar wind conditions have little effect on the magnetopause identification. The Solar wind Magnetosphere Ionosphere Link Explorer (SMILE) mission will provide X-ray images of the magnetopause for the first time, and our global hybrid-PIC simulation results can help better understand the 2-D X-ray images of the magnetopause from a 3-D perspective, with particle kinetic effects considered.

Keywords: magnetopause; X-ray emissivity; X-ray imaging; SMILE; global hybrid-PIC simulation

---

1. Introduction

When the solar wind interacts with the terrestrial magnetic field, the Earth's magnetopause is formed. The magnetopause, which was first predicted by Chapman and Bartels (1940), is an abrupt boundary between the magnetosphere and the magnetosheath. Many *in-situ* observations have provided abundant data to reveal physical processes locally at the magnetopause, including magnetopause reconnection (Dungey, 1961; Burch et al., 2016; Wang RS et al., 2017a) and flux transfer events (Russell and Elphic, 1978; Wang RS et al., 2017b; Wang SM et al., 2019). However, it is difficult to collect sufficient data, during a single spacecraft crossing, to build a coherent picture of the overall responses and evolutions of the magnetopause.

Discovery of the solar wind charge exchange (SWCX) X-ray emission (Lisse et al., 1996; Cravens, 1997; Bhardwaj et al., 2007), a novel method of soft X-ray imaging was proposed to remotely detect the large-scale magnetopause (Branduardi-Raymont et al., 2012; Collier et al., 2012; Walsh et al., 2016; Sibeck et al., 2018).

First author: J. Guo, gj0507@mail.ustc.edu.cn
Correspondence to: T. R. Sun, trsun@spaceweather.ac.cn
S. Lu, lusan@ustc.edu.cn
Received 20 FEB 2023; Accepted 22 MAY 2023.
First Published online 08 JUL 2023.
©2023 by Earth and Planetary Physics.

When highly charged heavy ions in the solar wind (such as O^{7+}) encounter and interact with neutral atoms and molecules (such as hydrogen) in the geospace environment, electrons can be transferred from the neutral atoms (or molecules) to the ions; such electron capture raises these ions from the solar wind to an electronically excited state. Later, when they decay to lower-energy states, the highly charged heavy ions emit one or more photons in the extreme ultraviolet or soft X-ray bands. In a region with dense solar wind ions and neutral atoms (or molecules), such as the magnetosheath and the cusps, the soft X-ray emissivity is expected to be strong. However, in the magnetosphere, where the plasma is tenuous, the soft X-ray emissivity is weak. Therefore, there is a sharp boundary at the magnetopause in terms of the soft X-ray emissivity, which means that images formed using a soft X-ray telescope can detect this boundary.

SWCX X-ray emissions have been observed by narrow-field-of-view (FOV) telescopes on board astronomical satellites (Fujimoto et al., 2007; Carter et al., 2011). The Soft X-ray Imager (SXI) that will fly onboard the Solar wind Magnetosphere Ionosphere Link Explorer (SMILE) mission will have a wide FOV (16° × 27°), capable of collecting the first X-ray images of the magnetopause and cusps (Branduardi-Raymont et al., 2016; Wang C et al., 2017; Wang C and Branduardi-Raymond, 2018). The SMILE mission, which is supported jointly by the European Space Agency and the Chinese Academy of Sciences, is expected to be launched in 2024 or 2025. Since no X-ray images of the large-scale terrestrial magnetopause have been observed so far, simulations of the magnetosheath are needed in order to be ready to analyze images expected from the SMILE mission. By using a numerical model, Robertson and Cravens (2003) first simulated X-ray images of the terrestrial magnetosheath under a given solar wind condition. Robertson et al. (2006) then used three-dimensional (3-D) magnetohydrodynamic (MHD) simulations to present the X-ray images of the magnetosheath including the cusps. Whittaker et al. (2016) analyzed the data from XMM-Newton observations to examine the accuracy of MHD modeling when describing the SWCX from the magnetosheath; they found that the MHD simulations are suitable for simulating the X-ray emissivity. Further, by performing global MHD simulations, the Kelvin-Helmholtz wave-induced X-ray emissivity at the low-latitude magnetopause (Sun TR et al. 2015) and the responses of the magnetopause and cusps to the solar wind changes (Sun TR et al., 2019) are studied. Recently, Sun TR et al. (2020) proposed the tangent fitting approach (TFA) to derive the magnetopause boundary. The TFA presents that the locations with maximum X-ray intensity on a soft X-ray image observed by an X-ray telescope (e.g., SMILE mission) correspond to the tangent directions of the magnetopause (Collier and Connor, 2018).

The Earth's magnetosheath, however, is turbulent because of many plasma waves, such as Alfvén ion cyclotron (AIC) waves and mirror waves caused by ion temperature anisotropy (Lacombe et al., 1990, 1992; Anderson et al., 1991; Fuselier et al., 1991; Anderson and Fuselier, 1993; Lu QM and Wang S, 2005, 2006; Alexandrova et al., 2006). Moreover, the magnetopause is also turbulent because of patchy, sporadic magnetic reconnection and the resultant flux transfer events (e.g., Russell and Elphic, 1978; Lee and Fu, 1985; Tan B et al., 2011; Guo J et al., 2021a). These effects are due to particle kinetics that cannot be resolved in the MHD simulations. However, global hybrid simulations, in which ions are treated as full particles while electrons are treated as a massless fluid, can describe ion kinetics in a global context (e.g., Lin Y and Wang XY, 2005; Lin Y et al., 2014; Lu S et al., 2015; Guo ZF et al., 2020; Guo J et al., 2021a). Therefore, in the turbulent environment with these particle kinetic effects, whether the magnetopause can still be identified needs to be verified by performing global hybrid simulations.

In this study, we present 3-D global hybrid-particle-in-cell (hybrid-PIC) simulations with southward interplanetary magnetic field to estimate the soft X-ray imaging of the terrestrial magnetosheath under different solar wind conditions. We find that the magnetopause boundary can be well-identified well, although there are large amplitude fluctuations of the X-ray emissivity in the magnetosheath. Solar wind conditions and satellite positions have little effect on magnetopause identification. In this paper, methods are described in Section 2; simulation results are presented in Section 3; conclusions and discussion are presented in Section 4.

2. Materials and Methods

2.1 Three-Dimensional Global Hybrid-PIC Simulation Model

In this study, we use a global hybrid-PIC simulation model (Swift, 1996; Lin Y and Wang XY, 2005; Guo J et al., 2021a) to study the soft X-ray imaging of Earth's magnetosheath. In this model, a spherical coordinate system (r, θ, φ) is used, and the geocentric solar-magnetospheric (GSM) coordinate is employed to describe the simulation results. The simulation domain contains the hemispherical plasma regions with GSM $x > 0$, within a geocentric distance $3\,R_{\rm E} \le r \le 24\,R_{\rm E}$ (where $R_{\rm E}$ is the Earth's radius); the Earth is located at $r = 0$. To avoid the singular coordinate line along the polar axes, a semicone of 20° polar angle around the positive and negative polar axes, which are chosen along the GSM $\pm y$ axes in the calculation, is cut out from the domain. While cutting a semicone polar angle around the positive and negative polar axes, the dayside cusps can be retained due to rotate the polar axis to the y axis. However, for the presentation, we use the conventional spherical coordinate system in which the polar angle ($0° < \theta < 180°$) is measured from the positive GSM z-axis, and the azimuthal angle ($20° < \varphi < 160°$) from the negative GSM y-axis. A total grid $N_r \times N_\varphi \times N_\theta = 400 \times 160 \times 200$ is used.

In this simulation model, ions are treated as particles, and electrons are treated as a massless fluid. Only protons are considered in the simulation. The equation for ion particle motion in the simulation is given as

$$\frac{{\rm d}\boldsymbol{v}_{\rm p}}{{\rm d}t} = \boldsymbol{E} + \boldsymbol{v}_{\rm p} \times \boldsymbol{B} - \upsilon\left(\boldsymbol{V}_{\rm p} - \boldsymbol{V}_{\rm e}\right), \tag{1}$$

where $V_{\rm p}$ is the ion particle velocity, $\boldsymbol{E}$ is the electric field in units of ion acceleration, $\boldsymbol{B}$ is the magnetic field in units of the ion gyrofrequency, υ is the collision frequency that is applied to the magnetopause for possible magnetic reconnection, and $V_{\rm p}$ and $V_{\rm e}$ are the bulk flow velocities of ion particles and electrons. The magnetic field is advanced in time using Faraday's law, the electric field is calculated from the electron momentum equation, and the flow velocity of electrons is derived from Ampère's law (refer to Lin Y and Wang XY, 2005 for a more detailed description).

In addition to the particle ions, a cold, incompressible ion fluid representing the plasmasphere is included in the inner magnetosphere. The number density of the cold ion fluid is assumed to be

$$N_f = \left(10^5/r^6\right) N_0, \tag{2}$$

where N_0 is the ion number density in the solar wind. For $r \geq 10\,R_E$, initially there are ion particles in the solar wind; the ion fluid density is set to be exactly zero.

To produce a higher resolution near the magnetopause, nonuniform grids are used in the r direction with a smaller grid size of $\Delta r \approx 0.03\,R_E$ limited to $8\,R_E \leq r \leq 14\,R_E$. Solar wind inflow boundary conditions are applied for the outer boundary at $r = 24\,R_E$, and outflow boundary conditions are utilized at the tailward boundary (corresponding to $x = 0$, and the two semiconic boundaries). The particles are reflected at the perfectly-conducting inner boundary located at $r = 3\,R_E$. Initially, a 3-D dipole magnetic field plus an image dipole is limited to $r \leq 10\,R_E$; they interact with the uniform solar wind placed in $r > 10\,R_E$. A transition layer (with a half-width of $1\,R_E$) exists between the dipole field and the IMF, centered at $r = 10\,R_E$. To guarantee that $\nabla \cdot \boldsymbol{B} = 0$ is satisfied, the initial setup of this method requires a correction of the initial $\boldsymbol{B}$ field. The Earth's dipole tilt angle is set to zero. The time step is $\Delta t = 0.02\,\Omega_i^{-1}$, where Ω_i is the unit ion gyrofrequency evaluated using the magnitude of the magnetic field in the solar wind. About 1×10^9 particles are used in each simulation.

Four cases (Cases 1–4) with different solar wind conditions and southward IMF are performed. In the solar wind, the number density N_{sw} and magnetic field B_{sw} of the four cases are shown in Table 1. The ion and electron plasma beta in the solar wind is $\beta_i = \beta_e = 0.6$. The solar wind is along the $-x$ direction, with a speed of 400 km/s; i.e., the Alfvén Mach number is $M_A = 11.6$ in Cases 1 and 3 (5.8, in Cases 2 and 4). In our simulations, we use $d_{i0} = 0.05R_E$ about six times larger than the realistic d_{i0} in Cases 1 and 3 (three times larger, in Cases 2 and 4). After such scaling, the size of Earth's dipole field and the magnetopause standoff distance are still real, and the Alfvén waves and FTEs can still be identified in the simulation results (e.g., Tan B et al., 2011; Shi F et al., 2013). This scaling of d_{i0} does not affect the global structure of the magnetosphere and the magnetopause identification after the line of sight (LOS) integral. In all cases, the inflow parameters are constant throughout the simulation. Each case required two hundred cores to run for about seven days.

Table 1. The four simulation cases presented in this study, with different solar wind conditions. Note that the IMF is the interplanetary magnetic field.

Case	Plasma density in the solar wind N_{i0} (cm^{-3})	IMF $\boldsymbol{B}_{swx}$ (nT)	IMF $\boldsymbol{B}_{swy}$ (nT)	IMF $\boldsymbol{B}_{swz}$ (nT)
1	20	0	0	−7.07
2	5	0	0	−7.07
3	20	0	5	−5
4	5	0	5	−5

2.2 Soft X-ray Intensity

All of the soft X-ray images presented in this study were derived from the 3-D global hybrid-PIC simulations described in Section 2.1. The soft X-ray intensity (I_X) along a given line of sight, calculated according to the model shown in Sun TR et al. (2015, 2019, 2021), is the line integration of the X-ray emissivity P_X:

$$I_X = \frac{1}{4\pi}\int P_X \mathrm{d}r = \frac{1}{4\pi}\int \alpha_X n_H n_{SW}\sqrt{u_{SW}^2 + u_{th}^2}\,\mathrm{d}r,$$

where α_X is the interaction efficiency factor; n_H is the number density of exospheric hydrogen; n_{sw} is the plasma number density in the solar wind; u_{sw} is the plasma bulk velocity; $u_{th} = \sqrt{3k_B T/m_i}$ is the plasma thermal speed (k_B is the Boltzmann's constant, T is the plasma temperature, and m_i is the ion mass). This equation expresses I_X in keV cm^{-2} s^{-1} sr^{-1}. In accordance with previous studies (Cravens, 2000; Pepino et al., 2004; Wargelin et al., 2014; Kuntz et al., 2015; Whittaker and Senmby, 2016), the value of α_X is set to $1 \times 10^{-15}\,\mathrm{eV\cdot cm^2}$ in this study, which is a conservative estimation given a solar wind speed of 400 km/s. The number density of exospheric hydrogen is represented as $n_H = n_0\,(10\,R_E/r)^3$ cm^{-3}, where $n_0 = 25$ is used in this study following previous studies (Hodges, 1994; Cravens et al., 2001; Sun TR et al., 2019; Connor and Carter, 2019; Fuselier et al., 2020).

3. Results

3.1 Tangent Directions of the Magnetopause and the Maximum X-ray Intensity

In Case 1, the interplanetary magnetic field (IMF) in the solar wind is purely southward, and the plasma number density in the solar wind is 20 cm^{-3}. The bow shock is formed in front of the Earth's magnetosphere at about t = 90 s because of the interaction between the solar wind and the magnetosphere. The magnetosheath, the magnetopause, and the cusps are well formed at about t = 140 s. Figure 1 plots the X-ray emissivity P_X at t = 471 s, 517 s, and 564 s in the noon-midnight meridian plane and in the equatorial plane. During this time interval, the magnetopause standoff distance is about $8.3\,R_E$, and the quasi-perpendicular shock standoff distance is about $10.8\,R_E$. The X-ray emissivity is high in the magnetosheath, whereas it is low in the magnetosphere and the solar wind. The polar cusps are funnel-shaped regions that connect the magnetosheath to the ionosphere (Heikkila, 1985). The X-ray emissivity is higher in the cusps than in the magnetosheath because the neutral atoms and molecules are dense in the cusps. In Figure 1, the X-ray emissivity in the magnetosheath is more fluctuating than that simulated by the MHD model (Sun TR et al., 2019) because there may be Alfvén ion cyclotron waves and mirror waves generated downstream of the quasi-perpendicular shock (Lee et al., 1988; Song P et al., 1994; McKean et al., 1995; Alexandrova et al., 2006). Moreover, there are elliptic regions with enhanced X-ray emissivity (red arrows in Figure 1) at the magnetopause. These enhanced X-ray emissivity regions are flux ropes (or flux transfer events, FTEs) formed at low latitude magnetopause, and they have enhanced plasma density and helical magnetic field lines (Figure 1c). The flux ropes are formed by the magnetopause reconnection (Russell and Elphic,

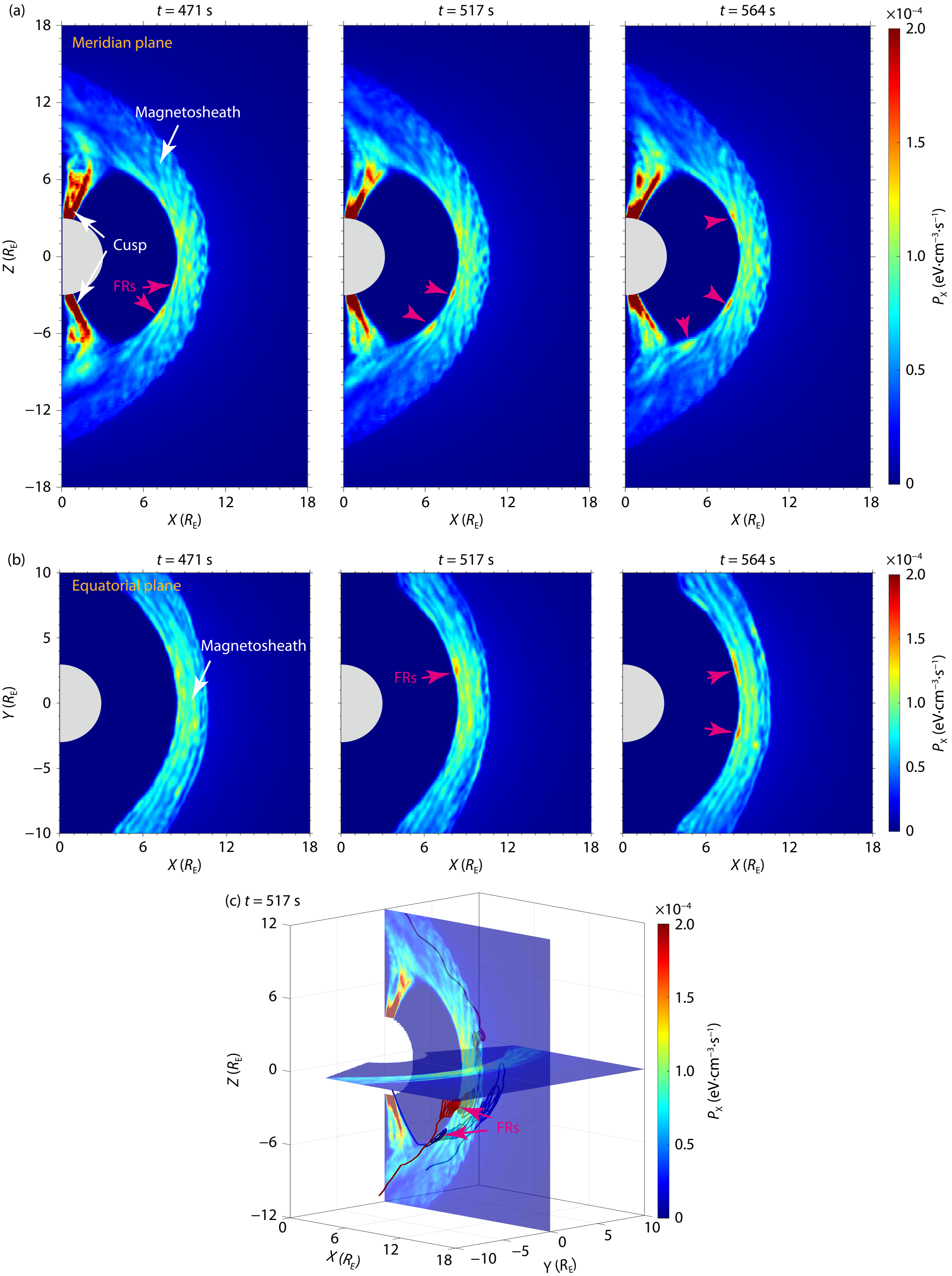

Figure 1. X-ray emissivity P_X at $t = 471$ s, 517 s, and 564 s, obtained from Case 1. (a) P_X in the noon-midnight meridian plane; (b) P_X in the equatorial plane; (c) 3-D view of P_X and flux ropes at $t = 517$ s. The two cusps and the magnetosheath are indicated by white arrows; the flux ropes are indicated by red arrows. The region within the inner boundary is indicated by the grey semicircle. In panel (c), the red and blue helical magnetic field lines represent two flux ropes.

1978; Tan B et al., 2011; Guo J et al., 2021a, b).

To evaluate how much the X-ray emissivity fluctuates in the magnetosheath, Figure 2 plots the average X-ray emissivity $\overline{P}_X$ in the LOS (panel a) and the fluctuation of X-ray emissivity $\left(P_X-\overline{P}_X\right)/\overline{P}_X$ (panel b) in the magnetosheath. The hypothetical satellite position $P1$ = (7.95, 0.32, 17.73) R_E is derived from the orbit data of the SMILE mission. In Figure 2b, the fluctuation of local X-ray emissivity (excluding the cusp regions), which may be caused by Alfvén ion cyclotron waves and mirror waves generated downstream of the quasi-perpendicular shock, can be up to 160% in the whole magnetosheath.

Figure 3 identifies the magnetopause boundary for Case 1 at t = 471 s. Figure 3a plots the 3-D magnetopause identified by finding the minimum gradient of B_z with the contour of X-ray emissivity P_X, and the red regions with enhanced X-ray emissivity are flux ropes. Among the LOS of the hypothetical satellite, the black LOS (Figure 3a) are tangent to the 3-D magnetopause. Figure 3b shows the X-ray intensity observed by a hypothetical satellite at position $P1$, plotted in the image coordinate system ($\theta-\varphi$, refer to Figure 2 in Sun TR et al., 2021). In the image coordinate system, the direction at (0, 0) is the telescope pointing direction, and the positive $\theta(\varphi)$ axis is oriented toward the Sun (dusk). The angular resolution of Figure 3a is 0.375°, which is lower than that of the SXI (about 0.135°–0.16°) onboard SMILE but sufficient to identify the magnetopause in this study. The red arc-like region with enhanced X-ray intensity is the magnetosheath and the magnetopause, and the two spots with enhanced X-ray intensity (denoted by white arrows) are the cusps. The northern cusp (denoted by "N") is on the left; on the right is the southern cusp (denoted by "S"). The tangent directions of the magnetopause in Figure 3a are corresponding to the black dots in Figure 3b, and the tangent directions match the maximum X-ray intensity (white dashed line) well. This indicates that the boundary and the shape of the magnetopause can be identified in the X-ray intensity images, even when there are significant fluctuations of X-ray emissivity in the magnetosheath (Figure 2). However, in Figure 3b the flux ropes are difficult to identify because they are obscured by the enhanced X-ray intensity of the magnetopause when they are at the low-latitude magnetopause. Figure 3c presents the spatial profiles of the X-ray intensity, as a function of φ = 0, at t = 471 s, 517 s, and 564 s. For the interval of 93 s, the magnetopause boundary (dashed line) changes from θ = 1.6° to 0.4° (x = 8.3 R_E to 7.9 R_E) in the image coordinate system (GSM coordinate). The magnetopause boundary change (0.4R_E) is smaller than the spatial resolution specified in the SMILE mission's scientific requirements, which include determining the boundary of the subsolar magnetopause to an accuracy better than 0.5 R_E (SMILE Science Study

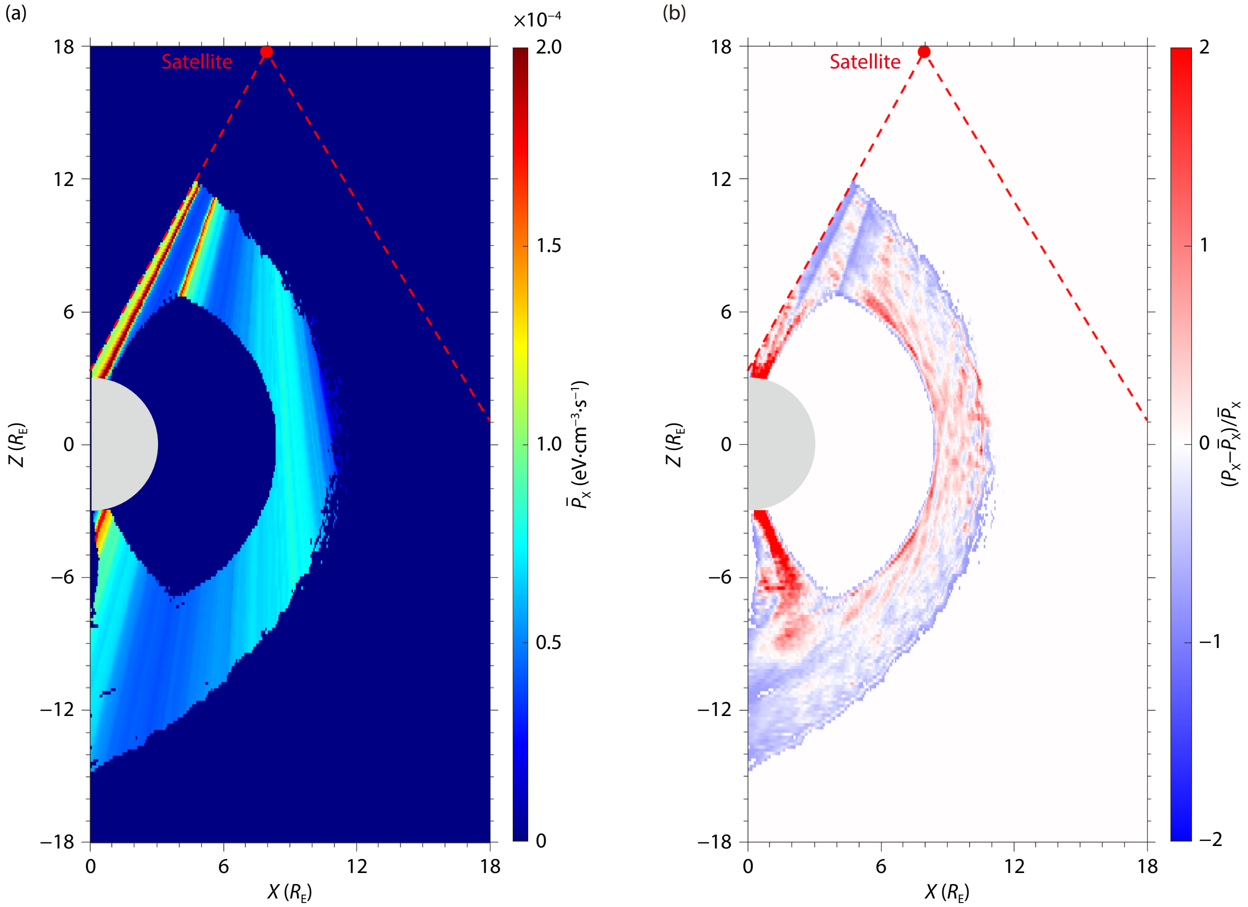

Figure 2. Fluctuation of X-ray emissivity in the noon-midnight meridian plane at t = 471 s, obtained from Case 1. (a) The average X-ray emissivity in line of sight (LOS) $\overline{P}_X$. Only the $\overline{P}_X$ values within the magnetosheath are shown; (b) The fluctuation of X-ray emissivity $\left(P_X-\overline{P}_X\right)/\overline{P}_X$. The position of a hypothetical satellite at $P1$ = (7.95, 0.32, 17.73) R_E is indicated by a red dot, and the hypothetical FOV in the meridian plane is indicated by dashed lines. The X-ray telescope points to (8.37, 0, 0) R_E. The region within the inner boundary is indicated by the grey semicircle.

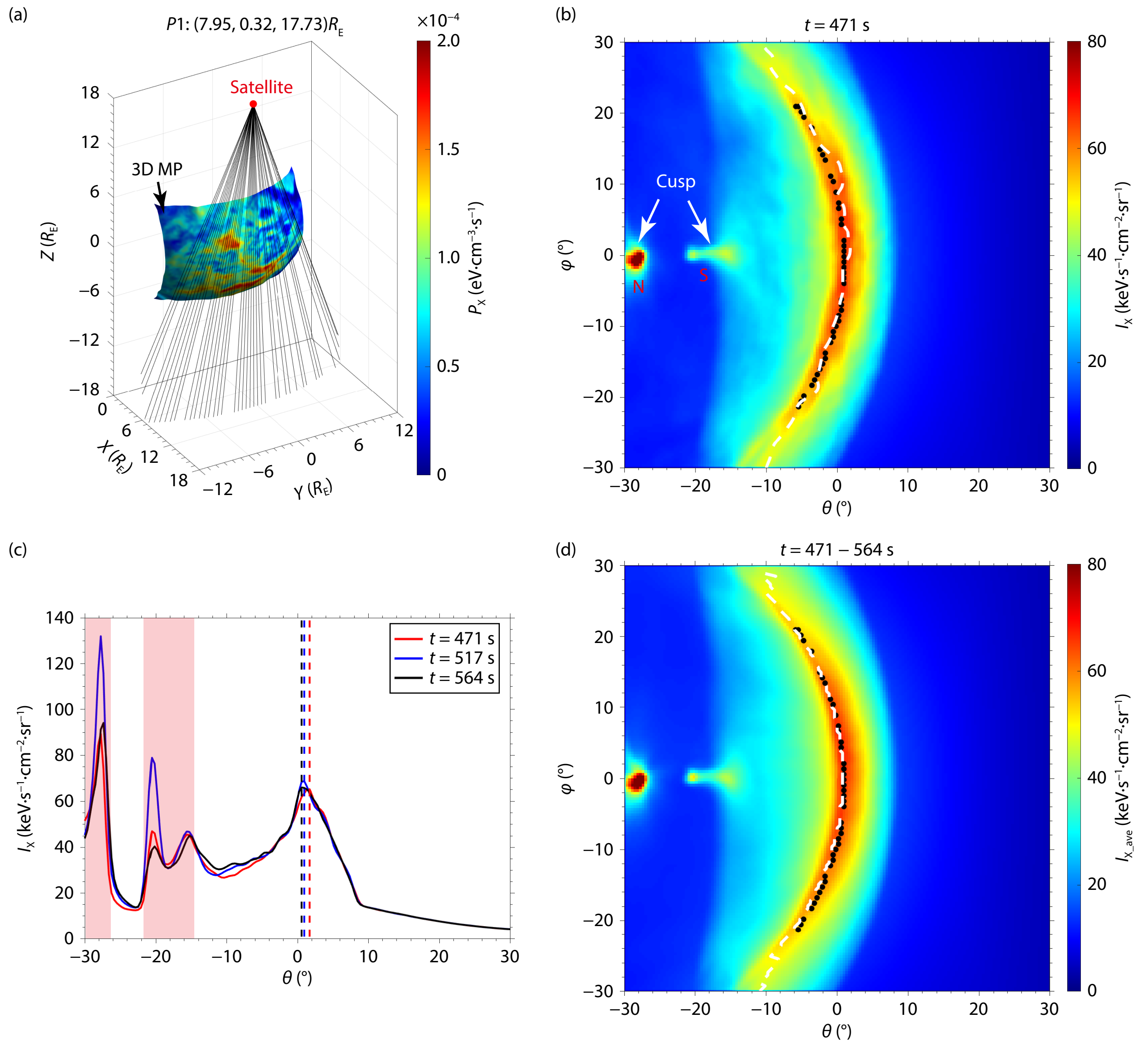

Figure 3. Magnetopause boundary identified at $t = 471$ s, obtained from Case 1. (a) The 3-D magnetopause with the contour of P_X (denoted by black arrow). Among the LOS of a hypothetical satellite, the black LOS are tangent to the magnetopause. The red dot represents the hypothetical satellite at $P1 = (7.95, 0.32, 17.73)\ R_E$. (b) The contour of soft X-ray intensity I_X, in the $\theta - \varphi$ image coordinate system. The white dashed line is the maximum I_X near the magnetopause; the black dots indicate the tangent directions of the magnetopause in panel (a). (c) Spatial profiles of the I_X, at $t = 471$ s, 517 s, and 564 s, as a function of $\varphi = 0$. The red-shadowed regions represent the cusps. The red, blue, and black dashed lines represent the magnetopause at $t = 471$ s, 517 s, and 564 s, respectively. (d) Time-averaged soft X-ray (I_{X_ave}) image from $t = 471$ to $t = 564$ s. The white dashed line is the maximum I_{X_ave} near the magnetopause; the black dots indicate the tangent directions of the magnetopause at $t = 471$ s.

Team, 2018). The left red-shadowed region is the northern cusp ($\theta - 28°$), and the right one is the southern cusp ($\theta - 18°$). Figure 3d plots the time-averaged soft X-ray image from $t = 471$ to $t = 564$ s. The perturbations of the maximum I_X in Figure 3b are blurred out, and the tangent directions match the maximum X-ray intensity better.

To estimate the influence of satellite positions on accuracy of magnetopause identification, Figure 4 plots the tangent directions, at $t = 471$ s, of the 3-D magnetopause and the X-ray intensity for different satellite positions. These positions are all derived from the candidate orbit of SMILE mission. Figure 4 reveals that the tangent directions of the 3-D magnetopause match the maximum X-ray intensity well, indicating that expected satellite positions should have little effect on magnetopause identification.

3.2 Influence of Different Solar Wind Conditions

Figure 5 displays the X-ray emissivity P_X under different solar wind conditions (Cases 2–4, at $t = 471$ s) in the noon-midnight meridian plane (panel a), and in the equatorial plane (panel b). X-ray emissivity is high when the plasma density in the solar wind is high (Cases 1 and 3). In Case 3, the magnetopause standoff distance is $8.4R_E$, which is similar to that in Case 1 because the solar wind dynamic pressure (about 5.4 nPa) is the same in both cases.

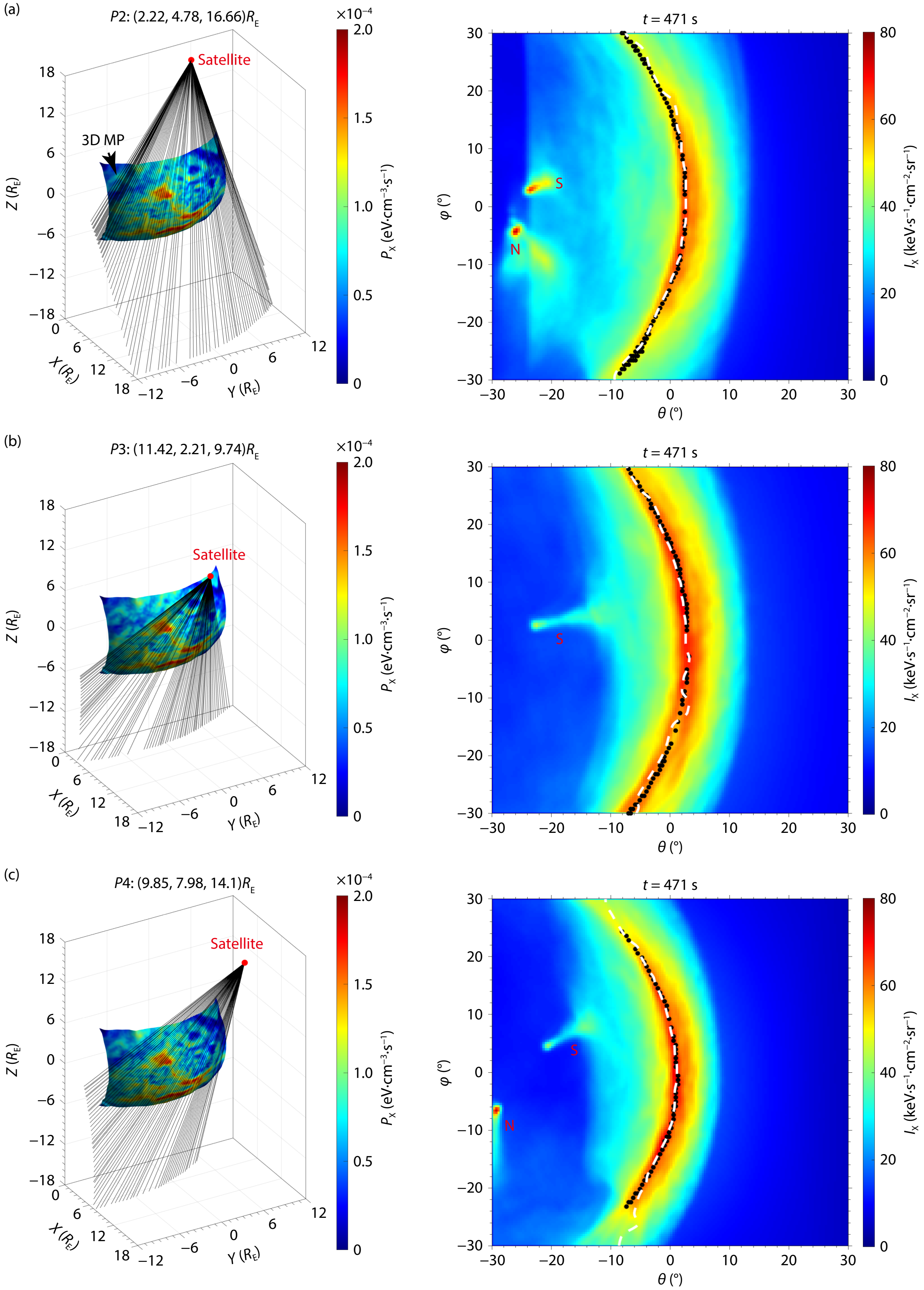

Figure 4. Magnetopause boundary identification at $t = 471$ s, from different satellite positions: in panel a, a hypothetical satellite is at $P2 = (2.22, 4.78, 16.66)$ R_E; in panel (b), its location is $P3 = (11.42, 2.21, 9.74)$ R_E; in panel (c), $P3 = (9.85, 7.98, 14.1)$ R_E. All other variables are in the same format as Figures 3a–b.

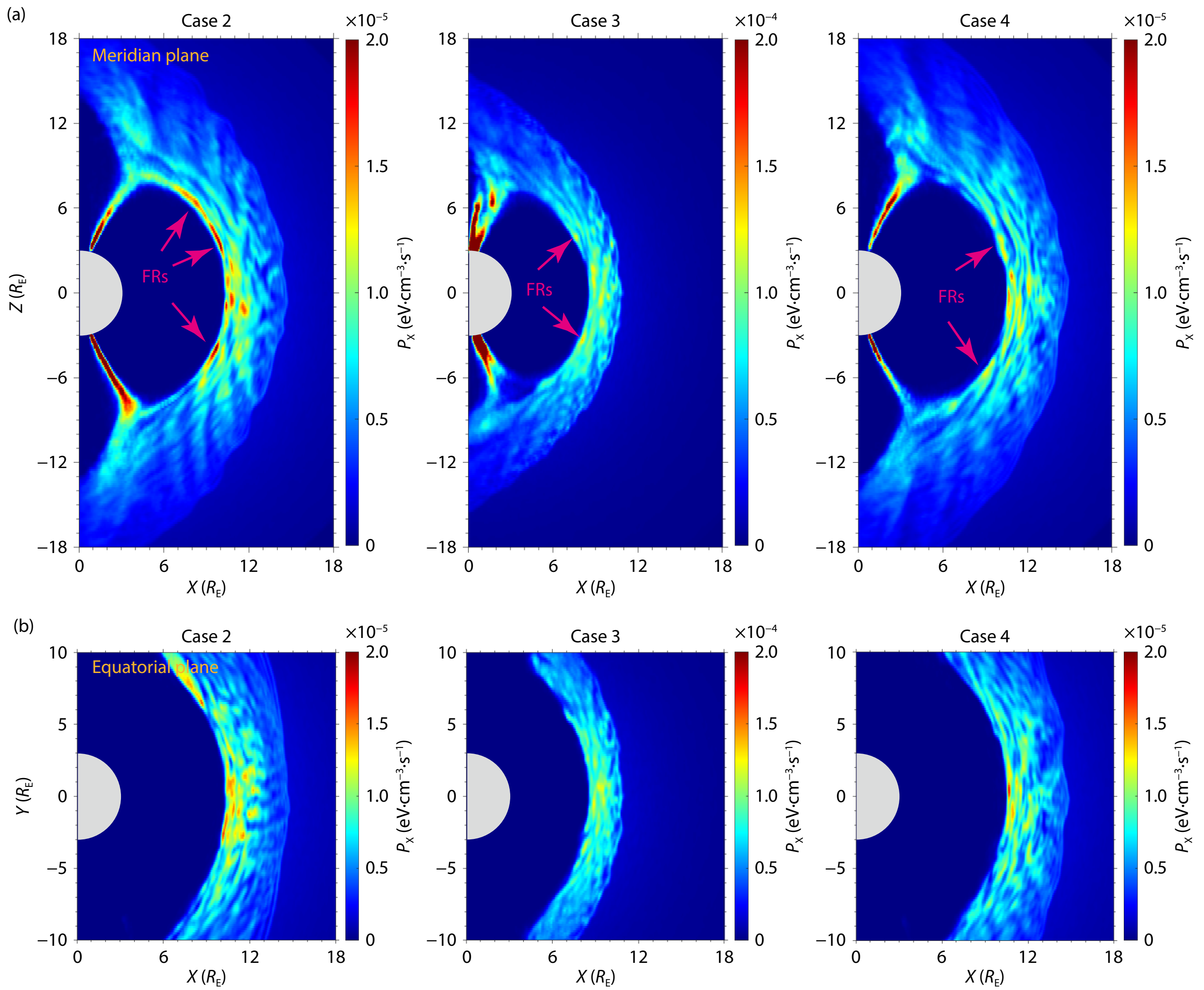

Figure 5. Comparison at $t = 471$ s of X-ray emissivity under different solar wind conditions, obtained from Cases 2–4: (a) P_X in the noon-midnight meridian plane. The red arrows represent the flux ropes; (b) P_X in the equatorial plane.

However, in Cases 2 and 4, the dynamic pressure is low (about 1.3 nPa) and the magnetopause standoff distances are 10.2 R_E and 10.4 R_E, respectively, larger than in Cases 1 and 3. When the IMF is southward, the magnetopause standoff distances r_0 can be expressed as an empirical formula $r_0 = (11.4 + 0.14B_{swz})(P_d)^{-1/6.6}$ (Shue et al., 1997), where P_d is the dynamic pressure in the solar wind. According to this empirical formula, the magnetopause standoff distances are 8.1 R_E in Case 1, 10.0 R_E in Case 2, 8.3 R_E in Case 3, and 10.3 R_E in Case 4, which are consistent with our simulation results. Moreover, the cusps are small when the solar wind dynamic pressure is low. In all cases, there are fluctuations of X-ray emissivity in the whole magnetosheath. When the IMF has a y component, the plasma density in the flux ropes is lower than when the IMF has no y component (Guo J et al., 2021a). In Case 3, the IMF y component is non-zero ($B_{swy} = 5$ nT and $B_{swz} = -5$ nT); the maximum X-ray emissivity in the flux ropes is $1.2 \times 10^{-4} \text{eV} \cdot \text{cm}^{-3} \cdot \text{s}^{-1}$, and the fluctuation of the X-ray emissivity relative to the average X-ray emissivity in LOS is about 130%. In Case 1, the IMF is purely southward; here the maximum X-ray emissivity in the flux ropes is $1.5 \times 10^{-4} \text{eV} \cdot \text{cm}^{-3} \cdot \text{s}^{-1}$, and the fluctuation of the X-ray emissivity relative to the average X-ray emissivity in LOS is about 160%, larger than that in Case 3.

Figure 6 plots the magnetopause tangent directions identified under different solar wind conditions (Cases 2–4). In Figure 6, the position of the hypothetical satellite is at $P1$, which is similar to that in Case 1 (Figure 3). The tangent directions of the 3-D magnetopause match the maximum X-ray intensity well in Cases 2 and 3 (Figures 6a and 6b). In Case 4, the tangent directions of the 3-D magnetopause deviate from the maximum X-ray intensity (Figure 6c) in some localized regions, while the general shape of the magnetopause is identified. The local deviations tend to be due to fluctuations in the magnetosheath, indicating that X-ray images may be able to reveal waves in the magnetosheath.

4. Discussion

In our simulation results, X-ray emissivity in the magnetosheath is

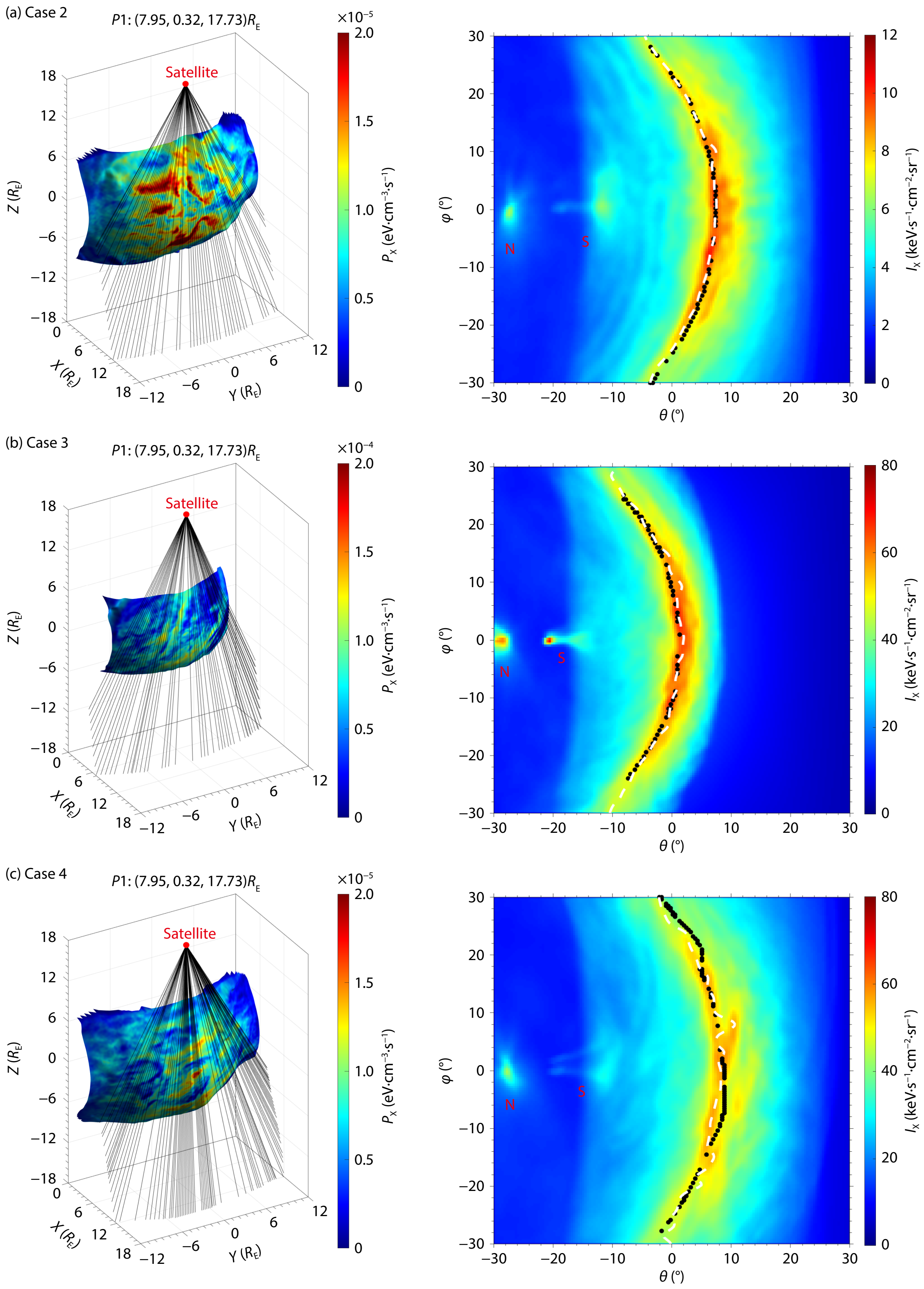

Figure 6. Magnetopause boundary identified under different solar wind conditions at $t = 471$ s. Panels (a–c) show Cases 2–4, respectively. The position of a hypothetical satellite is at $P1 = (7.95, 0.32, 17.73)$ R_E, which is similar to Figure 3. All other variables are in same format as Figures 3a–3b.

more fluctuating than in MHD model simulations (Sun TR et al., 2019) because there may be Alfvén ion cyclotron (AIC) waves and mirror waves generated downstream of the quasi-perpendicular shock (Lee et al., 1988; Song P et al., 1994; McKean et al., 1995; Alexandrova et al., 2006). Despite these magnetosheath X-ray emissivity fluctuations, the magnetopause boundary can still be identified in the 2-D X-ray images. It can be identified more clearly when the plasma in the solar wind is dense, and the IMF is purely southward, because the denser the solar wind plasma, the larger the X-ray emissivity in the magnetosheath (see Section 2.2), making it easier to identify the magnetopause. At the magnetopause, there are enhanced X-ray emissivity regions (Figures 1 and 5) which are flux ropes with high plasma density, formed by the magnetopause reconnection (Russell and Elphic, 1978; Tan B et al., 2011; Guo J et al., 2021a, b). The flux ropes are difficult to be identified in the 2-D X-ray images because they are obscured by the enhanced X-ray intensity of the magnetopause when they are at the low-latitude magnetopause. Special viewing geometries and image processing are required to identify the flux ropes in the 2-D X-ray images, which will be investigated in future work. These flux ropes with enhanced X-ray emissivity can increase the total X-ray intensity at the magnetopause in the 2-D X-ray images. When the IMF has a *y* component, the plasma density in the flux ropes is low (Guo J et al., 2021a), and there is no obvious enhanced X-ray emissivity in the flux ropes (Figure 5). We also note that fluctuations in the magnetosheath appear to correlate with local deviations between the magnetopause boundary and maximum X-ray intensity (Figure 6c), indicating that X-ray images may have potential to reveal waves in the magnetosheath. It requires further study. In summary, based on our hybrid-PIC simulation results, we believe the SMILE mission has considerable potential to provide X-ray images of the magnetopause that will give us a better understanding of Earth's magnetosphere.

In this study, only the cases with southward IMF are investigated. Under other IMF conditions, the magnetosheath and the magnetopause are very different. When the IMF has a strong *x* component (radial IMF), a quasi-parallel bow shock can be formed near the subsolar point of the Earth (Fairfield, 1971; Peredo et al., 1995; Lin Y, 2003; Lin Y and Wang XY, 2005; Guo J et al., 2022). Magnetic reconnection and high-speed jets can occur in the magnetosheath downstream of the quasi-parallel bow shock (e.g., Retinò et al., 2007; Hietala et al., 2009; Phan et al., 2018; Lu QM et al., 2019, 2021; Guo J et al., 2022), which further perturbs the turbulent magnetosheath. In this case, it is not clear whether the magnetopause boundary can be clearly identified. This question is worth further investigation. When the IMF is northward, the magnetic reconnection occurs at the high-latitude nightside magnetopause (Gosling et al., 1991; Lin Y and Wang XY, 2006; Hasegawa et al., 2008; Guo J et al., 2021c), and flux ropes cannot be formed at the dayside magnetopause. The magnetopause identification during the northward IMF remains in need of further study. Moreover, during time-varying solar wind conditions, the extent to which SMILE will be able to detect magnetopause displacement is also worth studying.

5. Conclusions

By performing 3-D global hybrid-PIC simulations, we study the soft X-ray emissions from SWCX in the Earth's magnetopause, magnetosheath, and cusps under different solar wind conditions. Results of our simulations involving ion kinetics suggest that, although there are large amplitude fluctuations (up to 160%) of the local X-ray emissivity in the whole magnetosheath, the maximum X-ray intensity matches well the tangent directions of the magnetopause, and the magnetopause boundary can still be identified in SMILE's 2-D X-ray images. Different positions of the satellite, and different solar wind conditions have limited effects on the general shape identification of the magnetopause.

Acknowledgments

Authors declare that they have no competing interests. This work was supported by the National Natural Science Foundation of China (NNSFC) grants 42074202, 42274196, Strategic Priority Research Program of Chinese Academy of Sciences grant XDB41000000, and ISSI-BJ International Team Interaction between magnetic reconnection and turbulence: From the Sun to the Earth. Computer resources were provided by the Hefei Advanced Computing Center of China. The authors gratefully acknowledge data resources from the "National Space Science Data Center, National Science & Technology Infrastructure of China." In this study, the simulation data used to plot the figures can be downloaded from https://doi.org/10.57760/sciencedb.o00009.00486.

References

Alexandrova, O., Mangeney, A., Maksimovic, M., Cornilleau-Wehrlin, N., Bosqued, J. M., and André, M. (2006). Alfvén vortex filaments observed in magnetosheath downstream of a quasi-perpendicular bow shock. *J. Geophys. Res.: Space Phys.*, *111*(A12), A12208. https://doi.org/10.1029/2006JA011934

Anderson, B. J., Fuselier, S. A., and Murr, D. (1991). Electromagnetic ion cyclotron waves observed in the plasma depletion layer. *Geophys. Res. Lett.*, *18*(11), 1955–1958. https://doi.org/10.1029/91GL02238

Anderson, B. J., and Fuselier, S. A. (1993). Magnetic pulsations from 0.1 to 4.0 Hz and associated plasma properties in the Earth's subsolar magnetosheath and plasma depletion layer. *J. Geophys. Res.: Space Phys.*, *98*(A2), 1461–1479. https://doi.org/10.1029/92JA02197

Bhardwaj, A., Elsner, R. F., Randall Gladstone, G., Cravens, T. E., Lisse, C. M., Dennerl, K., Branduardi-Raymont, G., Wargelin, B. J., Hunter Waite, J., … Kharchenko, V. (2007). X-rays from solar system objects. *Planet. Space Sci.*, *55*(9), 1135–1189. https://doi.org/10.1016/j.pss.2006.11.009

Branduardi-Raymont, G., Sembay, S. F., Eastwood, J. P., Sibeck, D. G., Abbey, T. A., Brown, P., Carter, J. A., Carr, C. M., Forsyth, C., … Yeoman, T. K. (2012). AXIOM: advanced X-ray imaging of the magnetosphere. *Exp. Astron.*, *33*(2), 403–443. https://doi.org/10.1007/s10686-011-92390

Branduardi-Raymont, G., Escoubet, C. P., Kuntz, K., Lui, T., Read, A., Sibeck, D., Sun, T. R., Walsh, B., and Wang, C. (2016). Link between solar wind, magnetosphere, and ionosphere. ISSI-BJ magazine, No.9.

Burch, J. L., Torbert, R. B., Phan, T. D., Chen, L. J., Moore, T. E., Ergun, R. E., Eastwood, J. P., Gershman, D. J., Cassak, P. A., … Chandler, M. (2016). Electron-scale measurements of magnetic reconnection in space. *Science*, *352*(6290), eaaf2939. https://doi.org/10.1126/science.aaf2939

Carter, J. A., Sembay, S., and Read, A. M. (2011). Identifying XMM-*Newton* observations affected by solar wind charge exchange—part II. *Astron. Astrophys.*, *527*, A115. https://doi.org/10.1051/0004-6361/201015817

Chapman, S., and Bartels, J. (1940). *Geomagnetism*. Oxford: Oxford University Press.

Collier, M. R., Porter, F. S., Sibeck, D. G., Carter, J. A., Chiao, M. P., Chornay, D., Cravens, T., Galeazzi, M., Keller, J. W., … Thomas, N. (2012). Prototyping a global soft X-ray imaging instrument for heliophysics, planetary science, and astrophysics science. *Astron. Nachr.*, *333*(4), 378–382. https://doi.org/10.1002/asna.201211662

Collier, M. R., and Connor, H. K. (2018). Magnetopause surface reconstruction from tangent vector observations. *J. Geophys. Res.: Space Phys.*, *123*(12), 10189–10199. https://doi.org/10.1029/2018JA025763

Connor, H. K., and Carter, J. A. (2019). Exospheric neutral hydrogen density at the nominal 10 R_E subsolar point deduced from XMM-Newton X-ray observations. *J. Geophys. Res.: Space Phys.*, *124*(3), 1612–1624. https://doi.org/10.1029/2018JA026187

Cravens, T. E. (1997). Comet Hyakutake X-ray source: charge transfer of solar wind heavy ions. *Geophys. Res. Lett.*, *24*(1), 105–108. https://doi.org/10.1029/96GL03780

Cravens, T. E. (2000). Heliospheric X-ray emission associated with charge transfer of the solar wind with interstellar neutrals. *Astrophys. J.*, *532*(2), L153–L156. https://doi.org/10.1086/312574

Cravens, T. E., Robertson, I. P., and Snowden, S. L. (2001). Temporal variations of geocoronal and heliospheric X-ray emission associated with the solar wind interaction with neutrals. *J. Geophys. Res.: Space Phys.*, *106*(A11), 24883–24892. https://doi.org/10.1029/2000JA000461

Dungey, J. W. (1961). Interplanetary magnetic field and the auroral zones. *Phys. Rev. Lett.*, *6*(2), 47–48. https://doi.org/10.1103/PhysRevLett.6.47

Fairfield, D. H. (1971). Average and unusual locations of the earth's magnetopause and bow shock. *J. Geophys. Res.*, *76*(28), 6700–6716. https://doi.org/10.1029/JA076i028p06700

Fujimoto, R., Mitsuda, K., McCammon, D., Takei, Y., Bauer, M., Ishisaki, Y., Porter, F. S., Yamaguchi, H., Hayashida, K., and Yamasaki, N. Y. (2007). Evidence for solar-wind charge-exchange X-ray emission from the earth's magnetosheath. *Publ. Astron. Soc. Jpn.*, *59*(S1), S133–S140. https://doi.org/10.1093/pasj/59.sp1.S133

Fuselier, S. A., Klumpar, D. M., Shelley, E. G., Anderson, B. J., and Coates, A. J. (1991). He^{2+} and H^{+} dynamics in the subsolar magnetosheath and plasma depletion layer. *J. Geophys. Res.: Space Phys.*, *96*(A12), 21095–21104. https://doi.org/10.1029/91JA02145

Fuselier, S. A., Dayeh, M. A., Galli, A., Funsten, H. O., Schwadron, N. A., Petrinec, S. M., Trattner, K. J., Mccomas, D. J., Burch, J. L., … Strangeway, R. J. (2020). Neutral atom imaging of the solar wind-magnetosphere-exosphere interaction near the subsolar magnetopause. *Geophys. Res. Lett.*, *47*(19), e2020GL089362. https://doi.org/10.1029/2020GL089362

Gosling, J. T., Thomsen, M. F., Bame, S. J., Elphic, R. C., and Russell, C. T. (1991). Observations of reconnection of interplanetary and lobe magnetic field lines at the high-latitude magnetopause. *J. Geophys. Res.: Space Phys.*, *96*(A8), 14097–14106. https://doi.org/10.1029/91JA01139

Guo, J., Lu, S., Lu, Q. M., Lin, Y., Wang, X. Y., Huang, K., Wang, R. S., and Wang, S. (2021a). Structure and coalescence of magnetopause flux ropes and their dependence on IMF clock angle: three-dimensional global hybrid simulations. *J. Geophys. Res.: Space Phys.*, *126*(2), e2020JA028670. https://doi.org/10.1029/2020JA028670

Guo, J., Lu, S., Lu, Q. M., Lin, Y., Wang, X. Y., Huang, K., Wang, R. S., and Wang, S. (2021b). Re-reconnection processes of magnetopause flux ropes: three-dimensional global hybrid simulations. *J. Geophys. Res.: Space Phys.*, *126*(6), e2021JA029388. https://doi.org/10.1029/2021JA029388

Guo, J., Lu, S., Lu, Q. M., Lin, Y., Wang, X. Y., Zhang, Q. H., Xing, Z. Y., Huang, K., Wang, R. S., and Wang, S. (2021c). Three-dimensional global hybrid simulations of high latitude magnetopause reconnection and flux ropes during the northward IMF. *Geophys. Res. Lett.*, *48*(21), e2021GL095003. https://doi.org/10.1029/2021GL095003

Guo, J., Lu, S., Lu, Q. M., Lin, Y., Wang, X. Y., Ren, J. Y., Hao, Y. F., Huang, K., Wang, R. S., and Gao, X. L. (2022). Large-scale high-speed jets in earth's magnetosheath: global hybrid simulations. *J. Geophys. Res.: Space Phys.*, *127*(6), e2022JA030477. https://doi.org/10.1029/2022JA030477

Guo, Z. F., Lin, Y., Wang, X. Y., Vines, S. K., Lee, S. H., and Chen, Y. X. (2020). Magnetopause reconnection as influenced by the dipole tilt under southward IMF conditions: hybrid simulation and MMS observation. *J. Geophys. Res.: Space Phys.*, *125*(9), e2020JA027795. https://doi.org/10.1029/2020JA027795

Hasegawa, H., Retinò, A., Vaivads, A., Khotyaintsev, Y., Nakamura, R., Takada, T., Miyashita, Y., Rème, H., and Lucek, E. A. (2008). Retreat and reformation of X-line during quasi-continuous tailward-of-the-cusp reconnection under northward IMF. *Geophys. Res. Lett.*, *35*(15), L15104. https://doi.org/10.1029/2008GL034767

Heikkila, W. J. (1985). Definition of the cusp. In J. A. Holtet, et al. (Eds.), *The Polar Cusp* (pp. 387-395). Dordrecht: Springer. https://doi.org/10.1007/978-94-009-5295-9_28

Hietala, H., Laitinen, T. V., Andréeová, K., Vainio, R., Vaivads, A., Palmroth, M., Pulkkinen, T. I., Koskinen, H. E. J., Lucek, E. A., and Rème, H. (2009). Supermagnetosonic jets behind a collisionless quasiparallel shock. *Phys. Rev. Lett.*, *103*(24), 245001. https://doi.org/10.1103/PhysRevLett.103.245001

Hodges, R. R. (1994). Monte Carlo simulation of the terrestrial hydrogen exosphere. *J. Geophys. Res.: Space Phys.*, *99*(A12), 23229–23247. https://doi.org/10.1029/94JA02183

Kuntz, K. D., Collado-Vega, Y. M., Collier, M. R., Connor, H. K., Cravens, T. E., Koutroumpa, D., Porter, F. S., Robertson, I. P., Sibeck, D. G., and Snowden, S. L. (2015). The solar wind charge-exchange production factor for hydrogen. *Astrophys. J.*, *808*(2), 143. https://doi.org/10.1088/0004-637X/808/2/143

Lacombe, C., Kinzelin, E., Harvey, C. C., Hubert, D., Mangeney, A., Elaoufir, J., Burgess, D., and Russell, C. T. (1990). Nature of the turbulence observed by ISEE 1-2 during a quasi-perpendicular crossing of the Earth's bow shock. *Ann. Geophys.*, *8*(7-8), 489–502.

Lacombe, C., Pantellini, F. G. E., Hubert, D., Harvey, C. C., Mangeney, A., Belmont, G., and Russell, C. T. (1992). Mirror and Alfvénic waves observed by ISEE 1-2 during crossings of the earth's bow shock. *Ann. Geophys.*, *10*(10), 772–784.

Lee, L. C., and Fu, Z. F. (1985). A theory of magnetic flux transfer at the earth's magnetopause. *Geophys. Res. Lett.*, *12*(2), 105–108. https://doi.org/10.1029/GL012i002p00105

Lee, L. C., Price, C. P., Wu, C. S., and Mandt, M. E. (1988). A study of mirror waves generated downstream of a quasi-perpendicular shock. *J. Geophys. Res.: Space Phys.*, *93*(A1), 247–250. https://doi.org/10.1029/JA093iA01p00247

Lin, Y. (2003). Global-scale simulation of foreshock structures at the quasi-parallel bow shock. *J. Geophys. Res.: Space Phys.*, *108*(A11), 1390. https://doi.org/10.1029/2003JA009991

Lin, Y., and Wang, X. Y. (2005). Three-dimensional global hybrid simulation of dayside dynamics associated with the quasi-parallel bow shock. *J. Geophys. Res.: Space Phys.*, *110*(A12), A12216. https://doi.org/10.1029/2005JA011243

Lin, Y., and Wang, X. Y. (2006). Formation of dayside low-latitude boundary layer under northward interplanetary magnetic field. *Geophys. Res. Lett.*, *33*(21), L21104. https://doi.org/10.1029/2006GL027736

Lin, Y., Wang, X. Y., Lu, S., Perez, J. D., and Lu, Q. (2014). Investigation of storm time magnetotail and ion injection using three-dimensional global hybrid simulation. *J. Geophys. Res.: Space Phys.*, *119*(9), 7413–7432. https://doi.org/10.1002/2014JA020005

Lisse, C. M., Dennerl, K., Englhauser, J., Harden, M., Marshall, F. E., Mumma, M. J., Petre, R., Pye, J. P., Ricketts, M. J., … West, R. G. (1996). Discovery of X-ray and extreme ultraviolet emission from comet C/Hyakutake 1996 B2. *Science*, *274*(5285), 205-209. https://doi.org/10.1126/science.274.5285.205

Lu, Q. M., and Wang, S. (2005). Formation of He^{2+} shell-like distributions downstream of the earth's bow shock. *Geophys. Res. Lett.*, *32*(3), L03111. https://doi.org/10.1029/2004GL021508

Lu, Q. M., and Wang, S. (2006). Electromagnetic waves downstream of quasi-perpendicular shocks. *J. Geophys. Res.: Space Phys.*, *111*(A5), A05204. https://doi.org/10.1029/2005JA011319

Lu, Q. M., Wang, H. Y., Wang, X. Y., Lu, S., Wang, R. S., Gao, X. L., and Wang, S. (2019). Turbulence-driven magnetic reconnection in the magnetosheath downstream of a quasi-parallel shock: a three-dimensional global hybrid simulation. *Geophys. Res. Lett.*, *47*(1), e2019GL085661. https://doi.org/10.1029/2019GL085661

Lu, Q. M., Yang, Z. W., Wang, H. Y., Wang, R. S., Huang, K., Lu, S., and Wang, S. (2021). Two-dimensional particle-in-cell simulation of magnetic reconnection in the downstream of a quasi-perpendicular shock. *Astrophys. J.*, *919*(1), 28. https://doi.org/10.3847/1538-4357/ac18c0

Lu, S., Lu, Q. M., Lin, Y., Wang, X. Y., Ge, Y. S., Wang, R. S., Zhou, M., Fu, H. S., Huang, C., … Wang, S. (2015). Dipolarization fronts as earthward propagating flux ropes: a three-dimensional global hybrid simulation. *J. Geophys. Res.: Space Phys.*, *120*(8), 6286–6300. https://doi.org/10.1002/2015JA021213

McKean, M. E., Omidi, N., and Krauss-Varban, D. (1995). Wave and ion evolution downstream of quasi-perpendicular bow shocks. *J. Geophys. Res.: Space Phys.*, *100*(A3), 3427–3437. https://doi.org/10.1029/94JA02529

Pepino, R., Kharchenko, V., Dalgarno, A., and Lallement, R. (2004). Spectra of the X-ray emission induced in the interaction between the solar wind and the heliospheric gas. *Astrophys. J.*, *617*(2), 1347–1352. https://doi.org/10.1086/425682

Peredo, M., Slavin, J. A., Mazur, E., and Curtis, S. A. (1995). Three-dimensional position and shape of the bow shock and their variation with Alfvénic, sonic and magnetosonic Mach numbers and interplanetary magnetic field orientation. *J. Geophys. Res.: Space Phys.*, *100*(A5), 7907–7916. https://doi.org/10.1029/94JA02545

Phan, T. D., Eastwood, J. P., Shay, M. A., Drake, J. F., Sonnerup, B. U. Ö., Fujimoto, M., Cassak, P. A., Øieroset, M., Burch, J. L., … Magnes, W. (2018). Electron magnetic reconnection without ion coupling in earth’s turbulent magnetosheath. *Nature*, *557*(7704), 202–206. https://doi.org/10.1038/s41586-018-0091-5

Retinò, A., Sundkvist, D., Vaivads, A., Mozer, F., André, M., and Owen, C. J. (2007). *In situ* evidence of magnetic reconnection in turbulent plasma. *Nat. Phys.*, *3*(4), 235–238. https://doi.org/10.1038/nphys574

Robertson, I. P., and Cravens, T. E. (2003). X-ray emission from the terrestrial magnetosheath. *Geophys. Res. Lett.*, *30*(8), 1439. https://doi.org/10.1029/2002GL016740

Robertson, I. P., Collier, M. R., Cravens, T. E., and Fok, M. C. (2006). X-ray emission from the terrestrial magnetosheath including the cusps. *J. Geophys. Res.: Space Phys.*, *111*(A12), A12105. https://doi.org/10.1029/2006JA011672

Russell, C. T., and Elphic, R. C. (1978). Initial ISEE magnetometer results: magnetopause observations. *Space Sci. Rev.*, *22*(6), 681–715. https://doi.org/10.1007/BF00212619

Shi, F., Lin, Y., and Wang, X. Y. (2013). Global hybrid simulation of mode conversion at the dayside magnetopause. *J. Geophys. Res.: Space Phys.*, *118*(10), 6176–6187. https://doi.org/10.1002/jgra.50587

Shue, J. H., Chao, J. K., Fu, H. C., Russell, C. T., Song, P., Khurana, K. K., and Singer, H. J. (1997). A new functional form to study the solar wind control of the magnetopause size and shape. *J. Geophys. Res.: Space Phys.*, *102*(A5), 9497–9511. https://doi.org/10.1029/97JA00196

Sibeck, D. G., Allen, R., Aryan, H., Bodewits, D., Brandt, P., Branduardi-Raymont, G., Brown, G., Carter, J. A., Collado-Vega, Y. M., … Wing, S. (2018). Imaging plasma density structures in the soft X-rays generated by solar wind charge exchange with neutrals. *Space Sci. Rev.*, *214*(4), 79. https://doi.org/10.1007/s11214-018-0504-7

SMILE Science Study Team. (2018). SMILE (solar wind magnetosphere ionosphere link explorer) definition study report, ESA/SCI.

Song, P., Russell, C. T., and Gary, S. P. (1994). Identification of low-frequency fluctuations in the terrestrial magnetosheath. *J. Geophys. Res.: Space Phys.*, *99*(A4), 6011–6025. https://doi.org/10.1029/93JA03300

Sun, T. R., Wang, C., Wei, F., and Sembay, S. (2015). X-ray imaging of Kelvin-Helmholtz waves at the magnetopause. *J. Geophys. Res.: Space Phys.*, *120*(1), 266–275. https://doi.org/10.1002/2014JA020497

Sun, T. R., Wang, C., Sembay, S. F., Lopez, R. E., Escoubet, C. P., Branduardi-Raymont, G., Zheng, J. H., Yu, X. Z., Guo, X. C., … Guo, Y. H. (2019). Soft X-ray imaging of the magnetosheath and cusps under different solar wind conditions: MHD simulations. *J. Geophys. Res.: Space Phys.*, *124*(4), 2435–2450. https://doi.org/10.1029/2018JA026093

Sun, T. R., Wang, C., Connor, H. K., Jorgensen, A. M., and Sembay, S. (2020). Deriving the magnetopause position from the soft X-ray image by using the tangent fitting approach. *J. Geophys. Res.: Space Phys.*, *125*(9), e2020JA028169. https://doi.org/10.1029/2020JA028169

Sun, T. R., Wang, X., and Wang, C. (2021). Tangent directions of the cusp boundary derived from the simulated soft X-ray image. *J. Geophys. Res.: Space Phys.*, *126*(3), e2020JA028314. https://doi.org/10.1029/2020JA028314

Swift, D. W. (1996). Use of a hybrid code for global-scale plasma simulation. *J. Comput. Phys.*, *126*(1), 109–121. https://doi.org/10.1006/jcph.1996.0124

Tan, B., Lin, Y., Perez, J. D., and Wang, X. Y. (2011). Global-scale hybrid simulation of dayside magnetic reconnection under southward IMF: structure and evolution of reconnection. *J. Geophys. Res.: Space Phys.*, *116*(A2), A02206. https://doi.org/10.1029/2010JA015580

Walsh, B. M., Collier, M. R., Kuntz, K. D., Porter, F. S., Sibeck, D. G., Snowden, S. L., Carter, J. A., Collado-Vega, Y., Connor, H. K., … Thomas, N. E. (2016). Wide field-of-view soft X-ray imaging for solar wind-magnetosphere interactions. *J. Geophys. Res.: Space Phys.*, *121*(4), 3353–3361. https://doi.org/10.1002/2016JA022348

Wang, C., Li, Z. J., Sun, T. R., Liu, Z. Q., Liu, J., Wu, Q., Zheng, J. H., and Li, J. (2017). SMILE satellite mission survey. *Space Int.* (*in Chinese*)(8), 13–16. https://doi.org/10.3969/j.issn.1009-2366.2017.08.003

Wang, C., and Branduardi-Raymond, G. (2018). Progress of solar wind magnetosphere ionosphere link explorer (SMILE) mission. *Chin. J. Space Sci.*, *38*(5), 657–661. https://doi.org/10.11728/cjss2018.05.657

Wang, R. S., Lu, Q. M., Nakamura, R., Baumjohann, W., Russell, C. T., Burch, J. L., Ergun, R. E., Lindqvist, P. A., Wang, S., … Gershman, D. (2017a). Interaction of magnetic flux ropes via magnetic reconnection observed at the magnetopause. *J. Geophys. Res.: Space Phys.*, *122*(10), 10436–10447. https://doi.org/10.1002/2017JA024482

Wang, R. S., Nakamura, R., Lu, Q. M., Baumjohann, W., Ergun, R. E., Burch, J. L., Volwerk, M., Varsani, A., Nakamura, T., … Wang, S. (2017b). Electron-scale quadrants of the hall magnetic field observed by the magnetospheric multiscale spacecraft during asymmetric reconnection. *Phys. Rev. Lett.*, *118*(17), 175101. https://doi.org/10.1103/PhysRevLett.118.175101

Wang, S. M., Wang, R. S., Yao, S. T., Lu, Q. M., Russell, C. T., and Wang, S. (2019). Anisotropic electron distributions and whistler waves in a series of the flux transfer events at the magnetopause. *J. Geophys. Res.: Space Phys.*, *124*(3), 1753–1769. https://doi.org/10.1029/2018JA026417

Wargelin, B. J., Kornbleuth, M., Martin, P. L., and Juda, M. (2014). Observation and modeling of geocoronal charge exchange X-ray emission during solar wind gusts. *Astrophys. J.*, *796*(1), 28. https://doi.org/10.1088/0004-637X/796/1/28

Whittaker, I. C., and Sembay, S. (2016). A comparison of empirical and experimental O^{7+}, O^{8+}, and O/H values, with applications to terrestrial solar wind charge exchange. *Geophys. Res. Lett.*, *43*(14), 7328–7337. https://doi.org/10.1002/2016GL069914

Whittaker, I. C., Sembay, S., Carter, J. A., Read, A. M., Milan, S. E., and Palmroth, M. (2016). Modeling the magnetospheric X-ray emission from solar wind charge exchange with verification from XMM-Newton observations. *J. Geophys. Res.: Space Phys.*, *121*(5), 4158–4179. https://doi.org/10.1002/2015JA022292